Lawrence Berkeley National Laboratory

Title
High-entropy alloy anode for direct internal steam reforming of methane in SOFC

Permalink
https://escholarship.org/uc/item/54p7k8c9

Journal
International Journal of Hydrogen Energy, 47(90)

ISSN
0360-3199

Authors
Lee, Kevin X
Hu, Boxun
Dubey, Pawan K
et al.

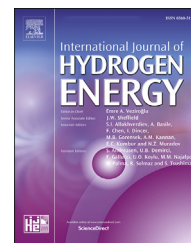**Publication Date**
2022-11-01

DOI
10.1016/j.ijhydene.2022.09.018

Peer reviewed

High-entropy alloy anode for direct internal steam reforming of methane in SOFC

Check for updates

Kevin X. Lee [a], Boxun Hu [b], Pawan K. Dubey [a], M.R. Anisur [a], Seraphim Belko [a], Ashish N. Aphale [c], Prabhakar Singh [a,*]

[a] Department of Materials Science and Engineering, University of Connecticut, Storrs, CT, USA
[b] Lawrence Berkeley National Laboratory, Berkley, CA, USA
[c] Department of Mechanical Engineering, Kennesaw University, Marietta GA, USA

HIGHLIGHTS

- Ni base anode allows endothermic cooling and carbon formation.
- HEA anode containing Cu, Ni, Co, Fe and Mn has been synthesized and electrochemically tested.
- HEA-GDC electrode showed carbon free and stable operation.

ARTICLE INFO

ABSTRACT

High-entropy alloy (HEA) anode and reforming catalyst, supported on gadolinium-doped ceria (GDC), have been synthesized and evaluated for the steam reforming of methane under SOFC operating conditions using a conventional fixed-bed catalytic reactor. As-synthesized HEA catalysts were subjected to various characterization techniques including N_2 adsorption/desorption analysis, SEM, XRD, TPR, TPO and TPD. The catalytic performance was evaluated in a quartz tube reactor over a temperature range of 700–800 °C, pressure of 1 atm, gas hourly space velocity (GHSV) of 45,000 h^{-1} and steam-to-carbon (S/C) ratio of 2. The conversion and H_2 yield were calculated and compared. HEA/GDC exhibited a lower conversion rate than those of Ni/YSZ and Ni/GDC at 700 °C, but showed superior stability without any sign of carbon deposition unlike Ni base catalyst. HEA/GDC was further evaluated as an anode in a SOFC test, which showed high electrochemical stability with a comparable current density obtained on Ni electrode. The SOFC reported low and stable electrode polarization. Post-test analysis of the cell showed the absence of carbon at and within the electrode. It is suggested that HEA/GDC exhibits inherent robustness, good carbon tolerance and stable catalytic activity,' which makes it a potential anode candidate for direct utilization of hydrocarbon fuels in SOFC applications.

Introduction

Solid oxide fuel cells (SOFCs) have successfully demonstrated flexibility of the utilization of multiples of fuels ranging from syn-gas, bio-gas, natural gas and other hydrocarbons to pure hydrogen [1,2]. Conventionally, hydrocarbons are externally reformed and reformate serves as fuel for electrochemical oxidation on the cell anode [3]. Direct internal reforming in SOFC, on the other hand, allows the hydrocarbons to be simultaneously reformed and electrochemically oxidized at the anode, resulting in high conversion and efficiency for electrochemical performance improvement, cost reduction and thermal management by combining exothermic oxidations with endothermic reformation reactions [4,5]. Ni-based anode in conventional SOFC provides high electronic conductivity and electrocatalytic activity, but suffers from excessive cooling and coke formation due to rapid endothermic reforming and thermal cracking of hydrocarbons [5,6]. This leads to a steep reduction in temperature especially at the inlet of the cell stack, resulting in a non-uniform temperature distribution along the cell [7,8]. A large temperature gradient along the cell surface may cause high mechanical instability and thermal stress between the anode and the solid electrolyte, leading to inevitable cell fracture and spallation [9]. Besides changes in the mechanical properties of cell and stack components leading to failure, the role of local temperature on subsequent reforming reaction and electrochemical reaction rates, as well as ionic conductivity of the electrolyte are influences and should not be overlooked [10]. To mitigate these challenges, significant efforts have been directed towards the development of electrochemically active anode materials with uniform temperature distribution and high coking resistance [11,12].

Hydrocarbons and reformate gas mixtures have been extensively used in commercial internal combustion engines and fuel cells for power generation [13]. Fig. 1 compares the energy densities of a number of sources of energy, where H_2 shows the largest mass energy density, but the lowest liquid volumetric energy density due to storage and transportation
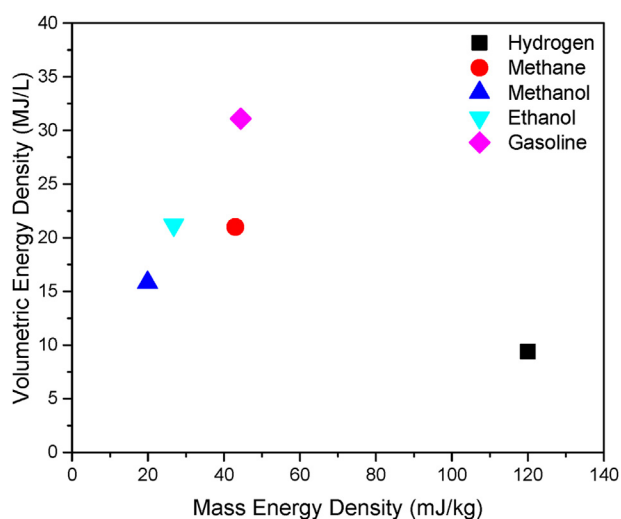

Fig. 1 — Comparison of mass and volumetric energy densities of various energy sources [18].

challenges. Approximately 95% of H_2 is currently being produced by steam reforming of methane (SRM) or partial oxidation of methane as well as gasification of coal [14,15]. Since a SOFC typically operates in the 600—1000 °C temperature range, relatively high operating temperature favors SRM on the cell. Additionally, the heat produced from the electrochemical reaction at the anode is used to promote the SRM reaction while the exothermic WGS reaction takes place concurrently to produce CO_2 and more H_2. Hence, the main advantages of utilizing internal steam reforming in SOFC include lower operational cost and higher thermal efficiency [16,17].

The choice of electrocatalyst catalyst and anode configuration plays an important role on the long term stability of fuel cell operation. That is, the catalyst must exhibit high catalytic activity and stability under industrial operating conditions. The state-of-the-art catalyst for SRM utilizes precious metals such as Pt and Rh, which are considerably expensive and scarce. Ni-based catalyst is widely used owing to its comparable reforming performance to that of precious metals [19] as well as cost effectiveness and availability [20]. Despite these advantages, Ni-based catalysts deteriorate very quickly due to Ni sintering and coking [21]. At such high temperatures during SRM, carbon formation can cause rapid catalyst deactivation. The two types of carbon that can form on a catalyst surface are encapsulated and filamentous carbons [22]. The latter, although does not deactivate the catalysts, is highly responsible for mechanical failure and increase pressure drop in the reactor, especially in SOFCs. Equation (1) represents carbon formation by CH_4 cracking. Subsequently, equation (2) refers to the Boudouard reaction, which is another possible route to form carbon during SRM.

$$CH_4 \rightarrow C + 2H_2 (\Delta H_{298°} = 76 kJ/mol) \tag{1}$$

$$2CO \rightarrow C + CO_2 (\Delta H_{298°} = -172 kJ/mol) \tag{2}$$
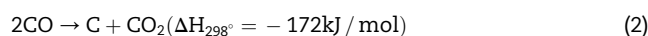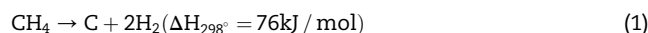
Studies have shown thermodynamically that increasing the S/C ratio can reduce coke deposition, consequently leading to higher conversion [23,24]. It is worth nothing, however, that the introduction of excess steam may lead to higher energy demand and operating cost, as well as lower H_2 yield [25].

To alleviate the aforementioned challenges faced with Ni anode and reforming catalyst, our approach focused on the development of multi constituent alloys, also known as high-entropy alloys (HEAs), as anode and SRM catalysts. HEAs are promising alloys that combine five or more metal elements to improve the catalytic and mechanical properties [26,27]. One metal of consideration is cobalt (Co). Reports indicate that Co exhibits relatively high affinity for oxygen species, which is beneficial for suppressing carbon formation [28,29]. Besides an effective oxidizing catalyst, it has been observed that Co also promotes WGS reaction to produce more syngas, while simultaneously inhibit the Boudouard reaction responsible for carbon formation [30]. Copper (Cu) is another common metal additive for SRM catalysts. Huang et al. demonstrated that the addition of Cu to Ni catalysts promotes the WGS reaction activity [31]. Despite this, Cu is known as a poor catalyst for C—C and C—H scission, thus slowing the rate of carbon formation [32]. DFT studies have confirmed that the incorporation of Cu

results in higher activation energy barrier (E_{act}) of carbon formation, while still maintaining an acceptable rate of reforming [33]. Hence, Cu is used to slow down the reforming rate, since the highly endothermic reaction could cause rapid cooling and consequently, thermal stress on the SOFC anode [5]. Besides chemical activity and stability, the SRM catalyst must also exhibit good physical stability and durability under industrial operating conditions. The use of Ni as an SOFC anode at high temperatures for long durations may undergo sintering and particle coarsening [34].

One plausible approach is to add metal additives with high melting point. Fe has been shown to be thermally stable at high temperatures, which makes it candidate for SOFC anode material [5]. Huang et al. reported that Fe possesses strong resistance against carbon formation during internal ethanol reforming in SOFC [35]. Due to the high affinity of Fe for oxygen species, the surface carbon can be easily oxidized to CO and subsequently CO_2 to avoid catalyst deactivation and further promote the WGS reaction. Similarly, manganese (Mn) has shown to be a beneficial oxidation catalyst without the risk of sintering or agglomeration [36]. This is advantageous as oxygen can transfer to the carbonaceous species and frees the surface from carbon deposition. Ouaguenouni et al. prepared a nickel-manganese oxide catalyst that exhibits good activity towards the complete oxidation of methane [37]. The ability of Mn to exist in different oxidation states makes it a good redox couple catalyst for SRM [38].

Table 1 summarizes the catalytic role of each metal in SRM and the corresponding drawbacks. In this study, the five metals discussed above have been consolidated in a solid solution known as the high-entropy alloy (HEA) as means to utilize the advantageous properties of each metal, while keeping thermal stress, endothermic cooling and rate of carbon formation minimal. Contrary to other fuel cell systems, the main challenge with SOFC does not concern with mass transfer or kinetics, but rather long term-stability, for which internal distributed reforming of hydrocarbon plays a key role. Long-term stable cell and stack operation require that the cell experience and possess distributed reforming and endothermic

cooling as well as resistance to carbon formation. By controlling the catalytic reaction of the anode, a thermal neutral state can be achieved as a result of both the endothermic steam reforming reaction and the exothermic electrochemical oxidation reactions [39,40]. It has been shown computationally using a 3D CFD model that the reforming rate should be reduced by a factor of 0.01 relative to that of Ni-based anode for a more uniform temperature distribution along the cell [41]. With the development of advanced anode, our objective is to reduce the reforming rate without significantly lowering the electrochemical activity of the cell, so that adequate current density can still be maintained. Thin film studies performed on sputter deposited above alloy compositions indicated the formation of solid solution (R. Bhattacharya, UES Inc. Personal communication). At elevated temperatures and under the SOFC operating conditions, it is envisioned that select alloy constituent can oxidize to form respective oxide based on the local oxygen partial pressure of the fuel. For the support, gadolinium- doped ceria (GDC) was used. CeO_2 is widely used as a support for SRM due to its oxygen storage capacity (OSC) to store and release oxygen species [42,43]. Additionally, Ce-based materials present high oxygen ion mobility that promotes carbon removal and hence, long-term stability of the cell [44]. The addition of Gd increases sintering resistance by enhancing the metal-support interaction [45]. HEAs with various metal contents supported on GDC were prepared and tested for SRM. Then, direct internal steam reforming in laboratory scale SOFC button cells were performed to examine the performance of HEA/GDC as a candidate anode. The reforming and electrochemical measurements, resistance to carbon formation were analyzed and compared to those of conventional Ni/YSZ and standard Ni/GDC anode.

Experimental

HEA powder synthesis

HEA was prepared using the co-precipitation method by dissolving optimized formulation of nitrate precursors obtained

Table 1 — Summary of advantages and disadvantages of some transition metals for SRM.

Metal	Advantages	Disadvantages	Ref.
Ni	• High SRM activity • Low cost	• Low resistance to sintering • Coke deposition	[3,24,46]
Co	• Strong affinity for oxygen • High resistance to sintering • Low coke formation • High WGS activity	• Unstable at high temperatures • Low reducibility	[28,30,47—50]
Cu	• Enhanced reducibility • High activity at low temperature • Low carbon formation • High WGS activity	• Poor H2 selectivity • Low melting point • Low resistance to sintering	[31,32,51—54]
Fe	• Strong affinity for oxygen • Low coke formation • High thermal stability • Low thermal expansion • High resistance to sintering	• Rapid oxidation • High dependency on pO2	[3,5,55]
Mn	• Strong affinity for oxygen • Low coke formation • High resistance to sintering	• Rapid oxidation • Low SRM activity	[37,38,56,57]

from Fisher Scientific (98% pure nickel (II) nitrate hexahydrate, 99% pure cobalt (II) nitrate hexahydrate, 99% pure copper (II) nitrate trihydrate, 98% iron (III) nitrate nonahydrtae and 98% manganese (II) nitrate tetrahydrate). A total of three different anode catalyst formulations were synthesized and tested for methane reforming, from which the alloy mixture with resistance to carbon formation and stable reforming was selected as the SRM catalyst for further bench-top and fuel cell studies. The resulting optimized formulation of the HEA anode is given in Table 2. The metal nitrates were dissolved in excess deionized (DI) water, stirred and heated to 90 °C. Then, citric acid (CA) was added as a chelating agent to the mixture using a 1.5:1 CA: metal ratio. Ammonium hydroxide (NH_4OH) solution was added dropwise to the metal-chelate solution to adjust the pH value to about 7–9 while stirring. The solution stirred overnight to homogenize the mixture and to evaporate excess water. On the next day, the remaining solution was transferred to an alumina crucible for calcination at the rate of 5 °C/min to 500 °C and held for 6 h to burn off nitrates, organic compounds and other contaminants. The as-obtained HEA powder and commercial 10% GDC (GDC-10 M) obtained from Fuelcell Materials USA were weighed (65:35 wt%) and physically mixed in a mortar and pestle until a homogenous mixture of fine powder was obtained. Table 2 provides the metal composition of each SRM catalyst for this study.

HEA characterization

N_2 adsorption/desorption analysis was conducted using a Micromeritics ASAP 2000 analyzer to determine the sample surface area, pore volume and pore distribution. Before the analysis, about 0.1 g of sample was outgassed for 12 h under vacuum in the degas port. Then, the sample was re-weighed to obtain the new moisture-free mass before starting the analysis. The measurement was carried out at 77 K under N_2 flow. The Brunauer-Emmett-Teller (BET) theory was then used to calculate the surface area. H_2 chemisorption was performed using the Micromeritics ASAP 2000C software to determine the metal dispersion. Powder X-ray diffraction (XRD) pattern of each sample was collected using a Bruker D8 Advance X-ray diffractometer to identify surface phases. The diffractometer was equipped with a Cu Kα radiation (λ = 0.15406 Å) operating at 40 kV and 40 mA. The XRD patterns were obtained in a 2θ range of 10–90°. The scanned XRD patterns were indexed using the ICDD (International center for Diffraction Data) database. Surface morphology and elemental composition of each sample before and after the SRM experiment were characterized using a FEI Quanta 250 FEG scanning electron microscope (SEM) coupled with energy dispersive E-ray spectroscopy (EDAX). H_2 temperature-programmed reduction (TPR), oxidation (TPO) and desorption (TPD) were carried out

on an Altamira Instruments AM1-200 unit. About 50 mg of sample was placed between quartz wool supports inside a U-shaped quartz tube. Prior to the TPR and TPD analyses, the sample was first pretreated in 10% O_2/He gas at a flow rate of 30 SCCM from 50 to 1000 °C and heating rate of 10 °C/min. TPD was carried out under inert atmosphere in pure Ar flow. Reduction experiments were performed using 50 SCCM of 10% H_2/Ar. After reduction, the gas feed was subsequently switched to 50 SCCM of 10% O_2/He for TPO study. All TPR, TPO and TPD studies were analyzed using a thermal conductivity detector (TCD). Inductively coupled plasma (ICP) with an optic emission spectroscopy (ICP-EOS) was used to quantify the bulk metal loadings of each catalyst. Post-test samples were also characterized for carbon formation by a Renishaw System 2000 equipped with a 514 nm green laser.

Reformation studies

The SRM test was performed in the temperature range of 700–800 °C at 1 atm and gas hourly space velocity (GHSV) of 45,000 h^{-1}.100 mg of SRM catalyst was loaded into a fixed-bed quartz tube with an outside diameter (OD) of ½" and a length of 38 cm as shown in Fig. 2. Both sides of the catalyst were supported by quartz wool. The reactor was then placed into a horizontal tube furnace. Prior to the test, the catalyst was first reduced in a constant 4% H_2/N_2 gas flow at 700 °C for 2 h. Then, the gas was switched to flow 10 SCCM of CH_4 and allowed to mix with 20 SCCM of H_2O inside an evaporator heated to 120 °C before entering the catalyst bed. H_2O was supplied by an HPLC pump at a flow rate of 0.016 mL/min to maintain a steam-to-carbon ratio (S/C) of 2.20 SCCM of N_2 was used as a carrier gas, amounting to a gas hourly space velocity (GHSV) of approximately 45,000 h^{-1}. Exhaust gas was condensed, collected and analyzed by a SRI 8610 gas chromatograph with a helium ionization detector (HID). Upon completion, the reactor and gas lines were purged with N_2 gas and then switched back to H_2 before cooling the reactor down to room temperature. The post-test samples were carefully removed from the quartz tube and quartz wool, and saved to be analyzed under SEM and Raman spectroscopy for any carbon deposition on the catalyst. The methane conversion (X_{CH4}) and hydrogen yield (Y_{H2}) were determined using equations (3) and (4), respectively. The rate of CH_4 consumption (r_{CH4}) normalized to the active metal loading was calculated by equation (5). A time-on-stream (TOS) test was conducted at 600 °C for 30 h to investigate the stability of SRM catalysts towards carbon poisoning. Except the operating temperature, the same operating conditions for the bench-top test was adopted. The TOS post-test samples were saved and analyzed using Raman spectroscopy. Additionally, surface morphology and elemental composition of post-test samples were characterized by SEM.

$$X_{CH4}(\%) = \frac{F_{CH4,in} - F_{CH4,out}}{F_{CH4,in}} \times 100\% \qquad (3)$$

$$Y_{H2}(\%) = \frac{F_{H2,out}}{2F_{CH4,in} + F_{H2O,in}} \times 100\% \qquad (4)$$

$$R_{CH4}\left(mol_{CH4}mol_{metal}^{-1}s^{-1}\right) = \frac{F_{CH4,in} - F_{CH4,out}}{N_{metal}} \qquad (5)$$

Table 2 – Select elements of each SRM catalyst and its metal composition.

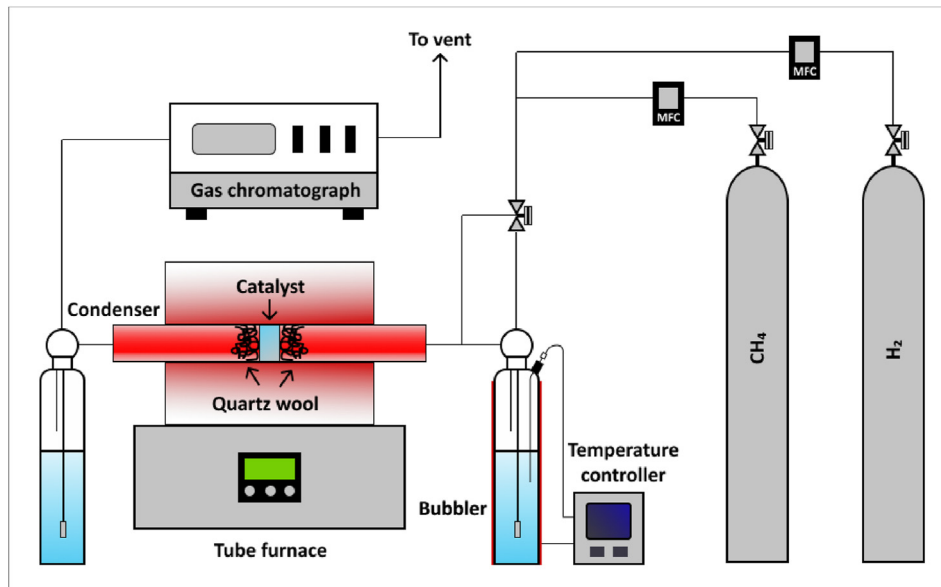| Catalyst	Ni (wt%)	Co (wt%)	Cu (wt%)	Fe (wt%)	Mn (wt%)
Ni/YSZ	65	0	0	0	0
Ni/GDC	50	0	0	0	0
HEA/GDC	9.75	13	16.25	16.25	9.75

Fig. 2 – Schematic of the experimental setup for SRM.

Where F_i is the molar flow rate of species i in mol/s and N_{metal} is the amount of active metal in moles.

Electrochemical studies

An electrochemical button cell (HEA/GDC - Ni/ScSZ|ScSZ|LSM/YSZ) was fabricated to examine the electrochemical performance of HEA/GDC as anode material for direct internal SOFC at 750 °C. Ni/ScSZ functional layer (10% Scandia stabilized zirconia purchased from Fuelcell Materials USA) was first deposited on the anode side and then sintered at 1350 °C for 2 h. This was followed by screen-printing LSM/YSZ cathode on the opposite side of the electrolyte and sintering at 1200 °C. The final anode layer of HEA/GDC was screen-printed on top of the anode functional layer and subsequently sintered at 1000 °C. The cell performance was evaluated at 750 °C on an in-house test station shown in Fig. 3. The cell was sealed using CeramaBond on one end of an alumina tube and the gold meshes were used as current collectors. To create a base line and reduce the anode, humidified hydrogen (9% H2–3% H2O–N2 bal.) was supplied to the anode side at a flow rate of 100 SCCM. The corresponding I vs. T for 3 h is shown in Fig. S1 in the supporting information. Subsequently, the gas was switched to CH_4 fuel with steam (S/C = 2) before entering the catalyst bed on the anode side. Unlike the bench-top experiment, a carrier gas was not used in this case to ensure low mass transfer resistance and maximum contact between the active area of the catalyst and methane. The resulting GHSV was similar to that used in the bench-top experiment. Then, the exhaust gas was condensed, collected and analyzed by the GC-HID. Air was fed through the cathode at a flow rate of 150 SCCM. The electrochemical test, similar to the bench top test, was carried out for 30 h. Current density and the electrochemical impedance spectra (EIS) measurements were
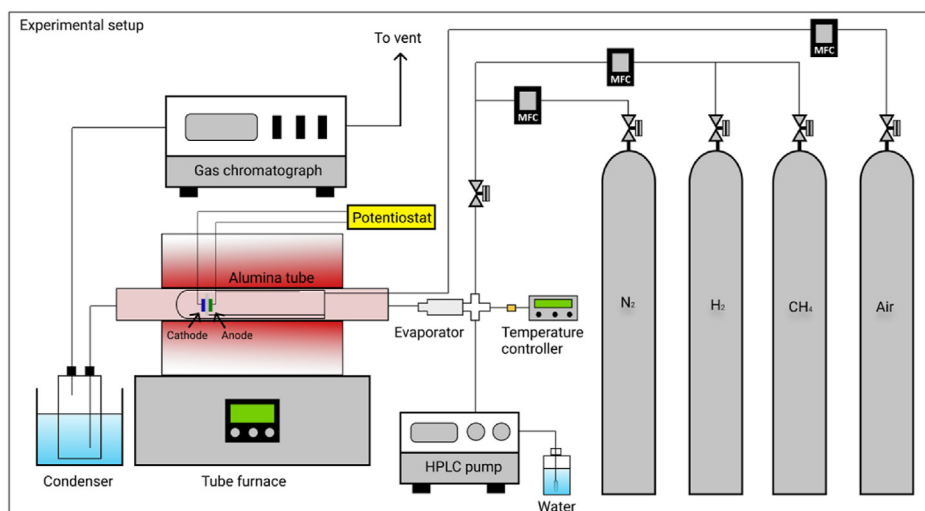

Fig. 3 – Schematic of the electrochemical test set up.

acquired at a constant voltage of 600 mV using a VMP3 Bio-Logic potentiostat/galvanostat. The frequency ranged from 10 mHz to 200 kHz, with 10 mV perturbation. For a more quantitative insight into the electrochemical phenomena, electrical equivalent circuit (EEC) $R_{\Omega}(QR_{HF})$ (QR_{LF}) was employed using ZSimpWin software to analyze the impedance data. The impedance of two interfaces metal/electrolyte and surface coating/electrolyte were analyzed to represent the two semicircles corresponding to the high and low-frequency arcs, respectively, which relate to gas adsorption–desorption on the electrode surface followed by charge transfer and incorporation of adsorbed gas at the three phase boundary, and the gas concentration polarization loss of the electrode. To investigate a carbon-free cell operation, SEM and Raman spectroscopy on the post-test cell were conducted.

Results and discussion

Physicochemical properties

In this study, the co-precipitation method was employed to synthesize the HEA anode material. To confirm if a single-phase alloy was formed, room-temperature powder XRD pattern was performed. Fig. 4(a) presents the XRD patterns of HEA/GDC as well as those of Ni/GDC and Ni/YSZ for comparison. The intensity of the XRD peaks is directly correlated to the crystallinity of the material. As expected, the crystallinity of reduced Ni/YSZ and Ni/GDC is more pronounced than that of the HEA/GDC due to less chemical and heat treatments of the former materials, thereby preserving the integrity of the crystal. Indexing by ICDD reveals that the catalysts were successfully reduced, as evidenced by the absence of oxide peaks. For the HEA/GDC catalyst, the denoted peaks are attributed to mixed metal alloys. This confirms that HEA was successfully synthesized without additional phases of oxides. The other diffraction peaks have also been indexed and confirmed by ICDD to denote the respective metal supports. Fig. 4(b) shows the N_2 adsorption/desorption isotherms of the SRM catalysts and the calculated BET surface area and pore volume are tabulated in Table 3,

along with other physicochemical properties. The linear relationship at the beginning of the isotherm, followed by a significant increase in the adsorption of N_2 indicates a type II physisorption isotherm, suggesting a nonporous structure. The addition of GDC as support increased the surface area. According to Angeli et al. the presence of CeO_2 improves the surface area and active metal dispersion [3]. Subsequently, the substitution of Ni with HEA supported on GDC further increased the surface area to 35 m^2/g due to enhanced pore size volume, which may enhance the catalytic properties of SRM.

SEM images of as-synthesized Ni/YSZ, Ni/GDC and HEA/GDC are shown in Fig. 5. The standard Ni/YSZ catalyst containing 45.2 wt% of Ni (Table 3) in difference resolutions is shown in Fig. 5(a–c). It can be seen that the Ni particles are relatively small and close to each other. H_2 chemisorption reported a Ni dispersion of 0.327% with a particle size of 310 nm. For Ni/GDC, the structures of NiO and GDC powders were dissimilar and could be easily distinguished from each other as seen in Fig. 5(d–f). The metal dispersion was slightly lower due to the increase in crystal size to 461 nm, which suggests that the increase in surface area could be attributed to the enhanced pore volume, owing to the GDC support. Fig. 5(g–i) show two distinct phases on HEA/GDC, arising from the presence of HEA and the GDC support. From the morphology, it can be seen that the particles tend to sinter and form larger agglomerates. This, however, changes as the HEA/GDC catalyst was reduced at higher temperature as the oxide phase converts into the FCC cubic phase, as shown by the XRD pattern in Fig. 4(a). Subjecting the catalyst to reduction may also result in higher porosity and smaller metal particles, leading to increased surface area.

TPR, TPO and TPD analyses

The coking resistance and SRM performance of a catalyst highly depends on interaction between the active metal and the support. Having a strong metal-support interaction in the catalyst suppresses metal sintering at elevated temperature and reduces coke formation, which in turn improves catalyst activity and stability [22,58]. To evaluate the chemical interaction between metal and support, the SRM catalysts were
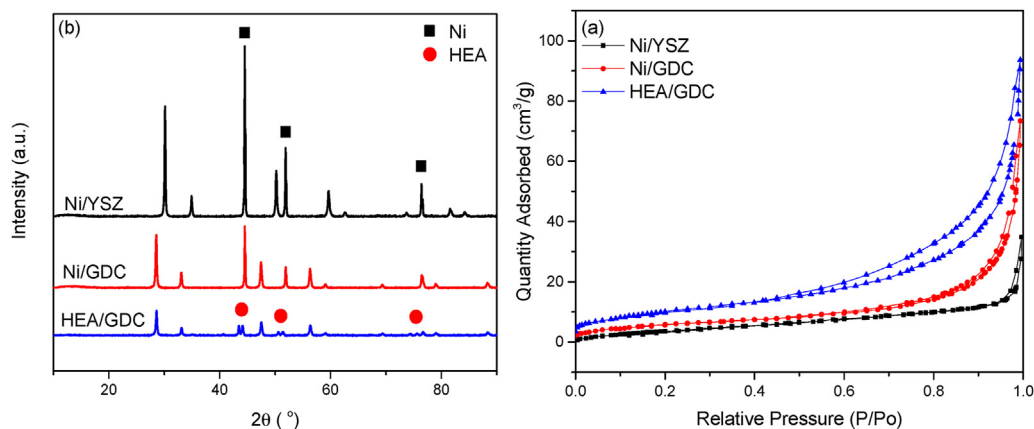

Fig. 4 – (a) XRD profiles of reduced SRM catalysts where (■) denotes reflection of Ni and (●) various solid solutions of HEA as well as (b) N_2 adsorption/desorption isotherms.

Catalyst	S_{BET} (m^2/g)	Pore volume (cm^3/g)	H$_2$ adsorbed[a] (μmol H$_2$/m^2)	O$_2$ desorbed[a] (μmol O$_2$/m^2)	TPD[a] (μmol O$_2$/m^2)	Metal loading[b] (wt %)	Metal dispersion[b] (%)	Crystal size[b] (nM)
Ni/YSZ	15.2	0.043	475.6	15.5	0	45.2	0.327	310
Ni/GDC	21.3	0.101	304.1	16.7	0	43.2	0.220	461
HEA/GDC	35.0	0.129	312.4	22.6	1.2	50.4	0.203	517

Table 3 − Physicochemical properties of SRM catalyst.

[a] H$_2$ adsorbed, O$_2$ desorbed under oxidizing condition and O$_2$ desorbed under inert condition determined by TPR, TPO and TPD, respectively.
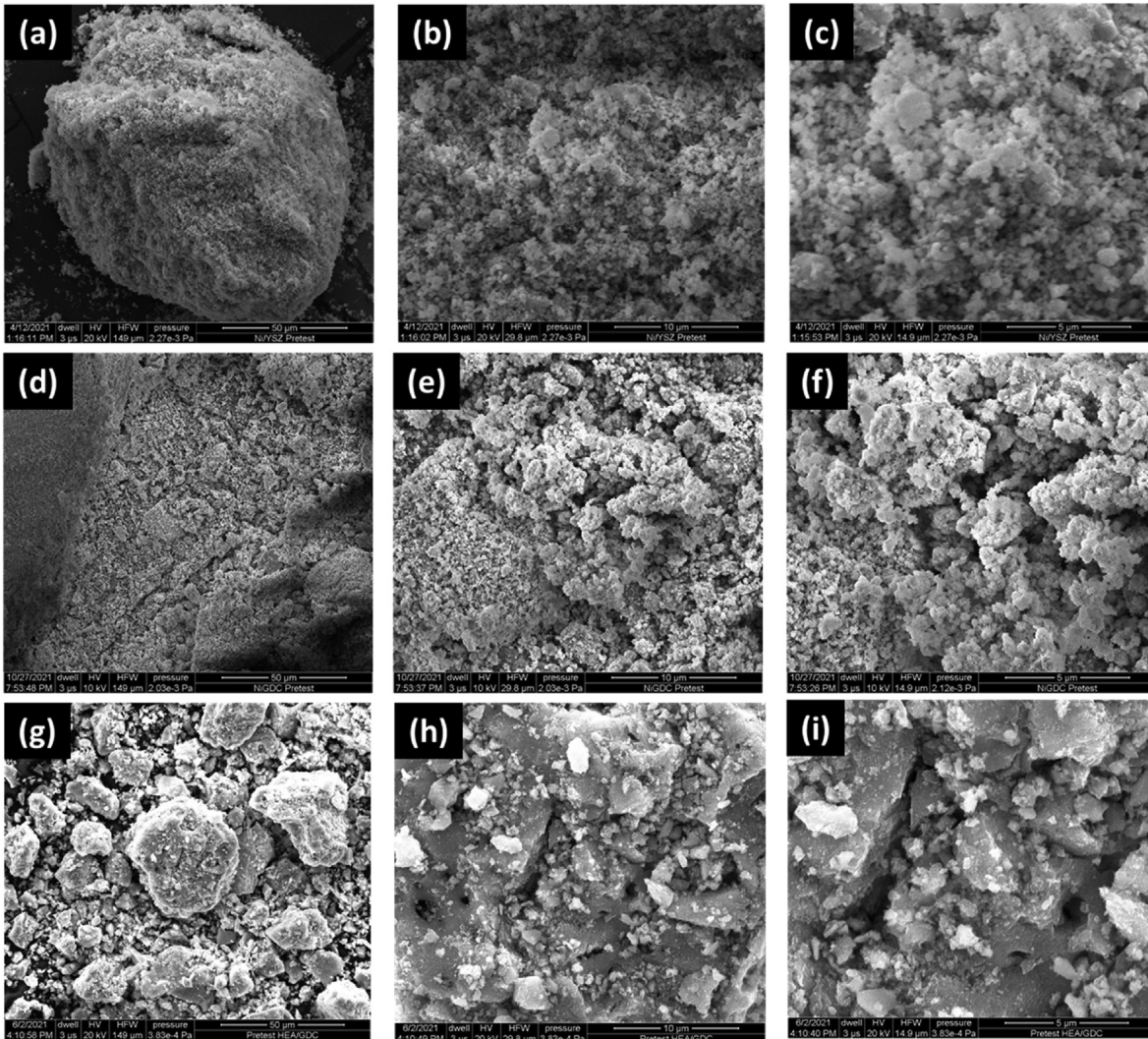[b] Metal loading, metal dispersion and crystal sized calculated by H$_2$ chemisorption.

Fig. 5 − SEM images of as-synthesized (a−c) Ni/YSZ, (d−f) Ni/GDC and (g−i) HEA/GDC.

analyzed by H$_2$-TPR as shown in Fig. 6(a). The reduction peak centered at 375 °C was assigned the reduction peak of NiO to Ni, which resulted from a weak interaction between Ni and the support [59]. During the TPR of HEA/GDC, it was observed that a broad peak emerged at 400 °C due to the reduction of the metal alloy. The reduction peaks of Co$_3$O$_4$ typically appear at approximately 400 °C and 470 °C, following a two-step reduction process to Co^0 [50]. Similarly, the two-step reduction of Mn$_2$O$_3$ to Mn$_3$O$_4$ and subsequently, to MnO would

result in reduction peaks at 300 °C and 420 °C, respectively [60]. Finally, the reduction of Fe$_2$O$_3$ to Fe also follows a two-step process, although the reduction of Fe$_3$O$_4$ to Fe^0 occurs at a much higher temperature of 835 °C [61]. The successful synthesis of HEA brings about a single-phase solid solution through which the compositions of five metals have been optimized. As a result, the properties of HEA are typically more superior than the corresponding metal counterparts. Such is the case in Fig. 6(a) showing that HEA/GDC requires a
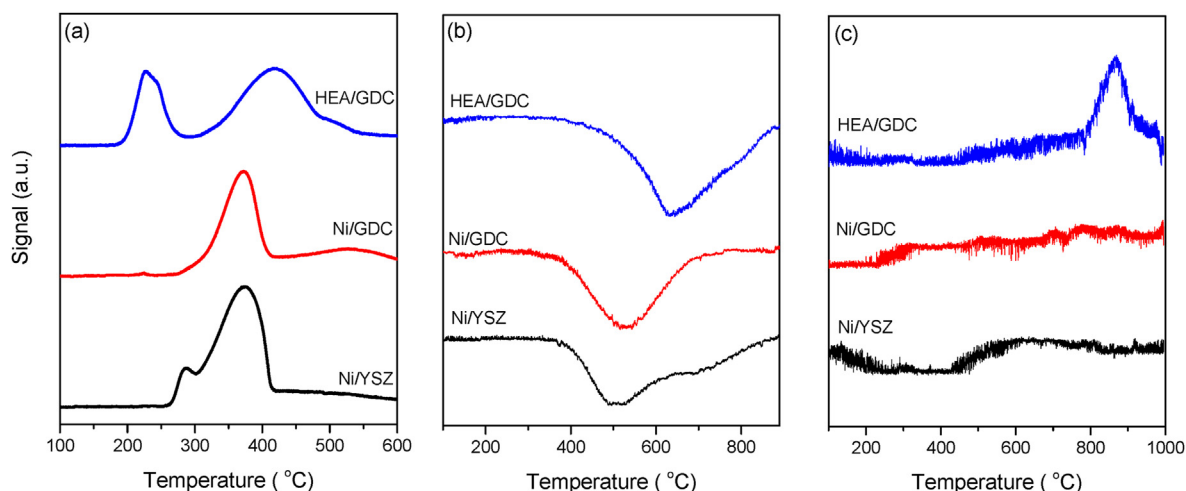
Fig. 6 – (a) TPR, (b) TPO and (c) TPD studies of SRM catalysts.

higher temperature for reduction compared with Ni/YSZ and Ni/GDC. Thus, the HEA/GDC catalyst should exhibit higher sintering and coking resistances. TPO of reduced samples is displayed in Fig. 6(b). Oxygen uptake appears to be minimal or non-existent, which can be explained by the rapid re-oxidation of metals and oxide supports during the switching between reducing and oxidizing gases. Nonetheless, the desorption of O_2 takes places at roughly 500 °C for Ni/YSZ and Ni/GDC, and ~600 °C for HEA catalysts under oxidizing conditions. The higher desorption temperature suggests a stronger interaction between HEA and oxygen. Fig. 6(c) displays the TPD results of samples after being subjected to oxygen pre-treatment. As expected, Ni/YSZ and Ni/GDC did not show any desorption of oxygen, while HEA/GDC exhibited a TPD peak at ~850 °C. This suggests that some HEA constituents such as Fe_2O_3 or Mn_2O_3 possess high oxygen storage capacity (OSC) and they have been proven beneficial for carbon removal. Quantification of TPO and TPD peaks of these samples in Table 3 shows that HEA/GDC is capable of adsorbing and desorbing a higher amount of oxygen, owing to the enhanced surface oxygen mobility and oxygen uptake of HEA and the GDC support [62].

Catalytic performance

The catalytic activity of SRM catalysts was examined using a fixed-bed tube reactor at varying operating temperatures of 700, 750 and 800 °C at a GHSV of 45,000 h^{-1}. At each temperature, the reaction was allowed to reach equilibrium, after which methane conversion was calculated and reported in Fig. 7(a). The main products in the exhaust were H_2, CO, CO_2 and CH_4. Water vapor in the exhaust was condensed before being fed to the GC. All SRM catalysts showed increasing conversion with temperature, with both nickel-based catalysts (Ni/YSZ and Ni/GDC) displaying the highest methane conversion at equilibrium. This is expected as the SRM reaction is endothermic and therefore, thermodynamically favorable at higher temperature. It is also worth mentioning that while partial oxidation of CH_4 may occur subsequently with steam reforming, our calculations show that the partial

pressure of O_2 is too low (i.e. ~ 10^{-17} atm) for CH_4 to undergo direct oxidation, consistent with other reports [63]. The lowest conversion was reported by HEA/GDC, which increased from 27% at 700 °C to 35% at 750 °C and then to 42% at 800 °C. Subsequently, the increase in conversion is accompanied by an increase in hydrogen yield with temperature, as displayed in Fig. 7(b). Among the HEA catalysts, HEA/GDC reported the highest conversion at each temperature. The H_2 yield was calculated by measuring the amount of H_2 produced with respect to theoretical amount of H_2 produced from maximum conversion of CH_4 and H_2O. In all cases, the H_2 yield increased with temperature with both Ni/YSZ and Ni/GDC displaying slightly higher H_2 yield than HEA/GDC. The rate of CH_4 consumption was also calculated and compared as shown in Fig. 7(c). The increased temperature enhanced the consumption rate of CH_4 for all SRM catalysts. Both Ni/YSZ and Ni/GDC catalysts showed the highest rate of ~3.5 mol$_{CH4}$ mol$_{Ni}^{-1}$ s^{-1} by 750 °C. The high activity of Ni in SRM has been well-documented in the literature. A strong endothermic reaction may induce large temperature gradient especially when operating the catalyst on a SOFC. Furthermore, a fast reforming reaction as displayed by the Ni-based catalysts may result in thermal stresses and mechanical failures, thus lowering the cell efficiency. The HEA/GDC catalyst, however, showed a lower reforming rate of ~1 mol mol$_{CH4}^{-1}$ mol$_{HEA}^{-1}$ s^{-1} at 750 °C, which may provide a smaller temperature gradient during concurrent reactions of heterogeneous catalysis and electrochemistry. Experimental results show that an optimized formulation of HEA has reduced the reforming rate of methane compared with highly endothermic Ni-based catalysts. Consequently, the cell life and current distribution can be maintained. This is more advantageous than standard Ni/YSZ as an anode material since the latter has shown to experience major drawbacks especially under harsh conditions such as coking, metal agglomeration, thermal stress, mechanical failure and poor redox stability [3]. While higher localized reformation rates may imply faster and higher production of H_2, the objective of the alloy anode development is largely to minimize localized cooling and carbon deposition.
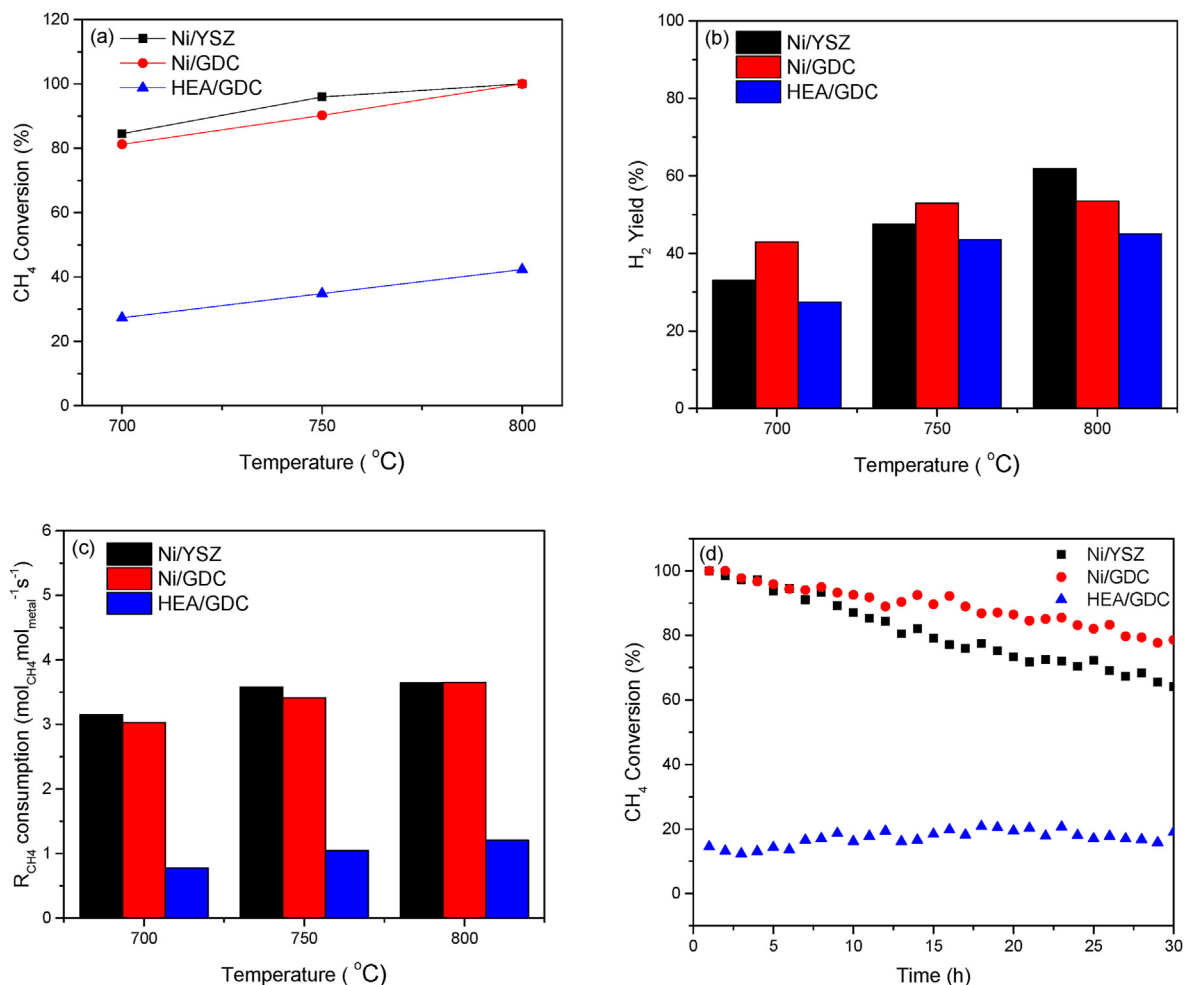
Fig. 7 − (a) Conversion of CH_4, (b) yield of H_2 and (c) equilibrium rate of CH_4 consumption over various SRM catalysts at reaction temperatures of 700, 750 and 800 °C, 1 atm, S/C = 2 and GHSV = 45,000 h^{-1}. (d) TOS experiment at 600 °C and S/C = 1 for 30 h.

Time-on-stream stability test

The catalytic stability of SRM catalysts was investigated at 600 °C and S/C ratio of 1. The TOS experiment was carried out isothermally for 30 h. Using the HSC® Chemistry 10 software, the equilibrium compositions were calculated for a temperature range of 25−1000 °C as shown in Fig. S2(a) in the Supporting Information. At 600 °C, the carbon activity should be at its highest and this temperature is thermodynamically favorable for studying carbon resistance of each SRM catalyst. Fig. 6(d) reports the conversion of CH_4 over time. It is evident that the initial conversion rate was high for both Ni/YSZ and Ni/GDC due to enhanced catalytic activity of Ni. However, the conversion gradually decreases over time with Ni/YSZ showing the fastest degradation rate, followed by Ni/GDC. After 30 h of TOS, the final conversions were 54% and 66% for Ni/YSZ and Ni/GDC, respectively. The higher stability of Ni/GDC suggests that the GDC support plays an important role in reducing catalyst deactivation. For the HEA/GDC catalyst, the conversion rate was relatively low compared to initial conversion rates of the standard catalysts, as shown in Fig. 6. Nonetheless, the catalyst maintained a stable run over 30 h of

TOS between 15 and 18% conversion, revealing the ability of HEA catalysts to resist deactivation over long periods of operation. To assess the source of catalyst deactivation, post-test catalysts were saved from TOS experiments and were subjected to Raman analysis and SEM imaging.

Characterization of SRM post-test samples

Carbon deposition has been regarded as one of the main reasons for catalyst deactivation during SRM. To identify the nature and structure of these surface carbonaceous species, post-test catalysts from the 30 h TOS test were subjected to SEM imaging. Fig. 8(a−c) show high resolution SEM images of post-test SRM catalysts after 30 h of TOS experiment. The surface of all samples appear to be free of any carbonaceous species. Post-test Ni/YSZ and Ni/GDC samples in Fig. 8(a and b) did not show any dissimilarities compared to their corresponding pre-test samples. HEA/GDC was observed to be more porous with a uniform distribution of particle size after reduction at 700 °C, consistent with relatively high BET surface area reported in Table 3. The absence of surface carbon on HEA/GDC in Fig. 8(c) may explain the promising stability
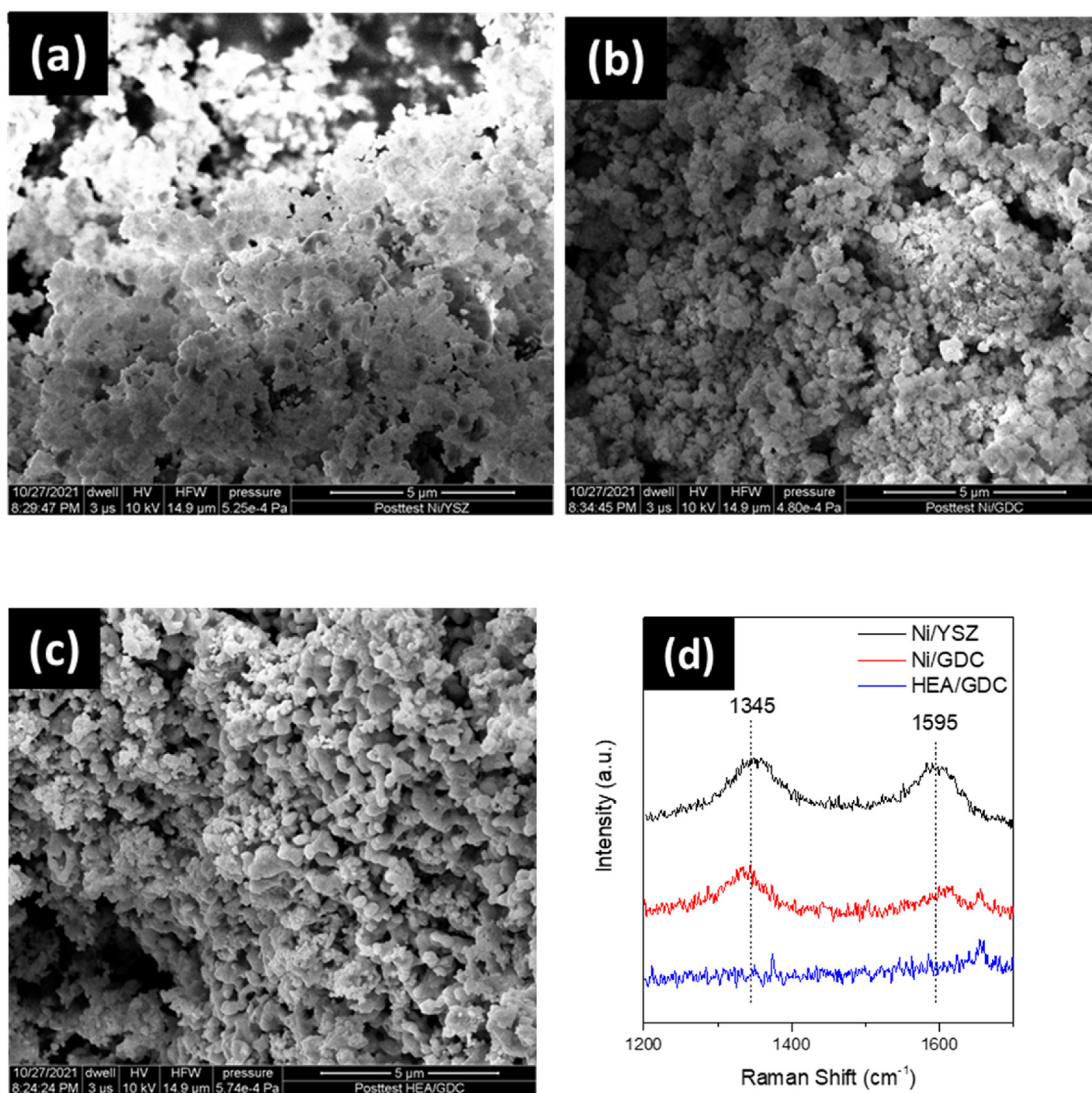
Fig. 8 — SEM images of post-test (a) Ni/YSZ, (b) Ni/GDC and HEA/GDC catalysts after 30 h TOS experiment. (d) Raman spectroscopy of post-test samples after 30 h TOS experiment.

during the 30 h of TOS. To confirm this and to further investigate the deactivation of the former two Ni-based catalysts, Raman spectroscopy was performed on all post-test samples. As shown in Fig. 8(d), all SRM catalysts showed two distinct characteristic peaks at 1345 and 1595 cm^{-1}. The peak at 1335 cm^{-1} can be attributed to the D band of carbonaceous species, formed by the vibrations of disordered carbon atoms (amorphous carbon for example), while the peak at 1595 cm^{-1} has been assigned the G band to represent the presence of ordered and graphitic crystalline structure caused by vibration of the in-plane sp [2]-bonded carbons [64]. Amorphous carbon has been shown to play a significant role in catalyst deactivation via encapsulation of the metal active sites [65]. On the other hand, graphitic carbon with filamentous structure may also form as a result of migration of surface carbon to the bulk metal phase, resulting in nucleation growth of carbon on the other side of the metal particle [21]. While graphitic carbon may not directly affect the activity of the catalyst, uncontrolled growth of carbon whiskers may result

in reactor blockage and pressure drop [66]. Additionally, coke formation on the anode material of a SOFC can be detrimental to the long-term stability of the system and could potentially lead to mechanical failure [12]. In Fig. 8(d), Ni/YSZ catalyst showed the highest amount of both amorphous and graphitic carbons on the surface, leading to catalyst deactivation during the 30 h TOS test as demonstrated in Fig. 7(d). Similarly, Ni/GDC exhibited some amorphous and graphitic carbonaceous species, which explains the gradual deactivation of the catalyst. The enhanced stability of HEA/GDC during TOS was due to the high carbon resistance of the catalyst, as both post-test SEM and Raman analyses did not show signs of carbon.

Electrochemical performance

The electrocatalytic activity and stability of (HEA/GDC-Ni/ScSZ|ScSZ|LSM/YSZ) for direct internal SOFC have been investigated. The moderate reformation rate and high long-term stability of the anode catalyst may prove beneficial in a
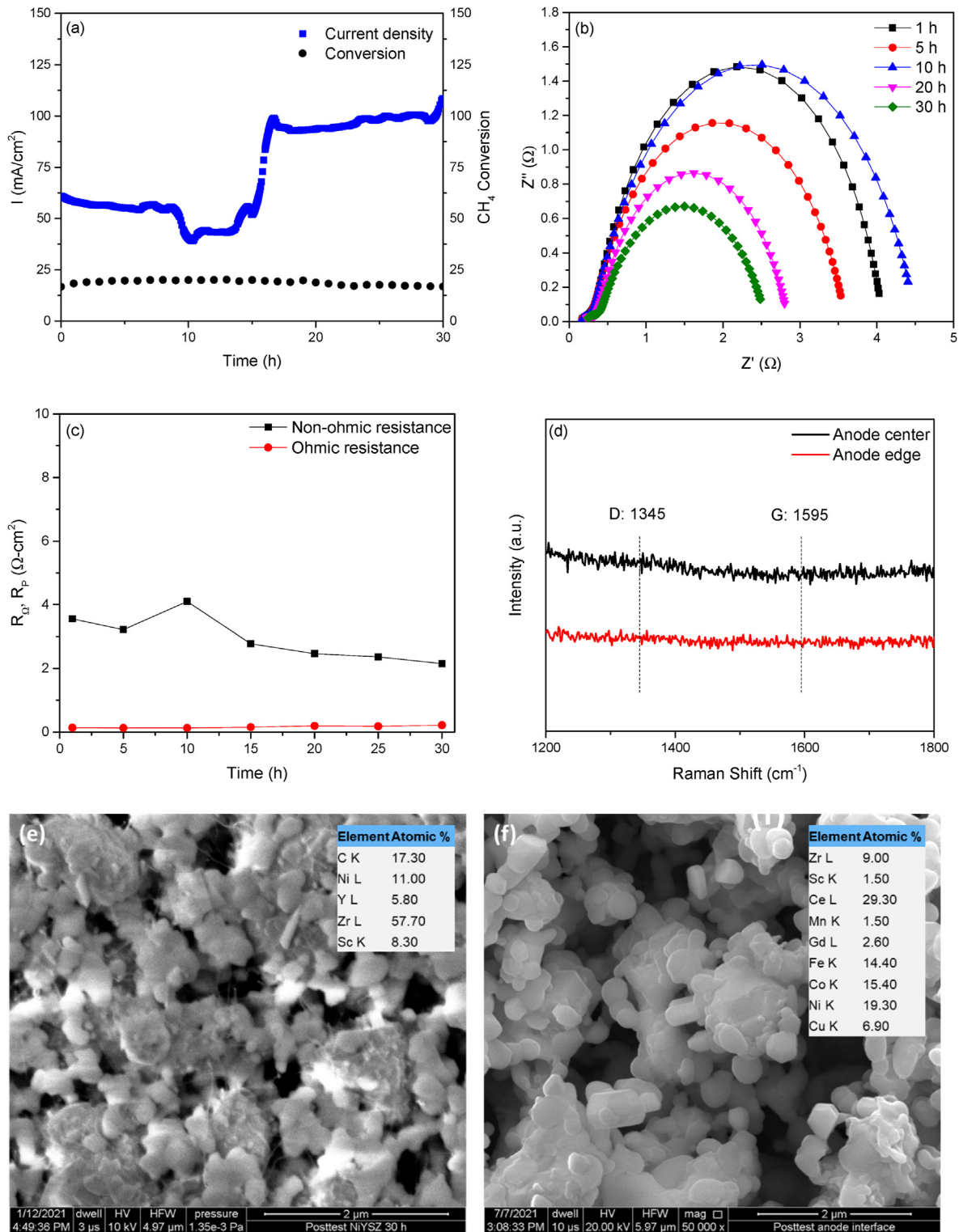
Fig. 9 — **(a) Electrochemical and catalytic data over 30 h of cell test with 0.6 V bias, (b) corresponding EIS data, (c) variation of ohmic and non-ohmic polarization with time, and (d) Raman analysis and (e) (f) SEM images of post-test SOFC anodes.**

SOFC system by preventing mechanical failures due to rapid temperature change and carbon deposition [5,12]. In this study, the cell test was performed at 750 °C, to which the anode was subjected a constant flow of CH_4 and steam (S/C = ~2) and the cathode with air. Under reduced atmosphere

and internal reforming condition, the open-circuit voltage (OCV) was measured to be ~0.9 V at 750 °C due to favorable interfacial interaction between the HEA/GDC anode layer and the ScSz electrolyte later after high-temperature sintering. The OCV plots can be found in Fig. S3. Upon switching the feed
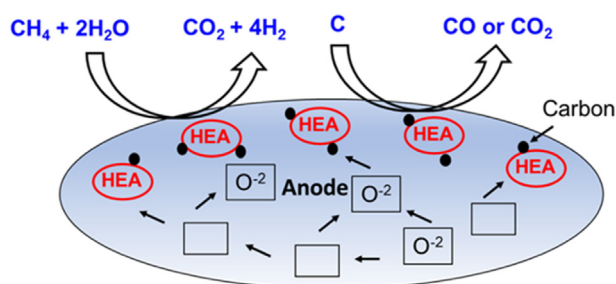
Fig. 10 – Schematic of HEA/GDC as anode in SOFC.

to CH_4 fuel and imposing a bias of 0.6 V, the I-T electrochemical data was collected for 30 h of SOFC test, as shown in Fig. 9(a). A slight dip in current density was noticed after 8 h of testing, which could be attributed to lower reformation rate, condensation of steam in cold zones of the inlet and diffusion of transition metals in the anode that could affect the ionic resistance of the cell [67]. This self-activation phenomenon has also been reported elsewhere as a result of surface modification on the anode during steam reforming [68,69]. During this time, the initial reforming rate is extremely low. However, upon reduction and activation, the reforming rate increases, leading to an increase in performance and current density. As soon as the HEA/GDC anode was fully activated after the first 15 h, the reforming rate was enhanced leading to an increase in current density to ~100 mA/cm^2 for the next 15 h. In comparison, the current density of a Ni-based anode was reported to be ~250 mA/cm^2 at the start of the cell operation, but quickly approached 0 mA/cm^2 due to carbon formation [63]. The relatively low current density may be due to electrolyte thickness, whose role on electrochemical performance will be explored in future work. Nonetheless, the HEA/GDC anode yielded sufficient current density to maintain a stable and carbon-free operation. This confirms that controlled and distributed reforming also improved the current density distribution in the cell. A more comprehensive electrochemical study involving dual atmosphere cycling to compare the current densities in reducing atmosphere and hydrocarbon-rich atmosphere will be considered in the future. The corresponding Nyquist spectra in Fig. 9(b) acquired at the different times are composed of two depressed semicircles which correspond to the polarization resistance Rp (R_{HF} + R_{LF}) while the high frequency intercept with the real impedance axis corresponds to the purely ohmic resistance (R_Ω) of the electrolyte and current collecting wires. As demonstrated in Fig. 9(c), the overall non-ohmic resistance R_p (R_{HF} + R_{LF}) decreases after 15 h indicating higher mass transfer due to increase in hydrocarbon reformation rate. The ohmic resistance remains stable during internal reforming indicating stable and carbon-free cell operation. The exhaust was simultaneously analyzed by a GC-HID and the conversion of CH_4 over 30 h of testing is shown in Fig. 9(a). The conversion of CH_4 was stable at 20% throughout the whole electrochemical test, which is consistent with the results obtained from the bench top experiments (Fig. 7). This is a good indication that the cell test is stable and scalable for future long-term testing.

Once the cell test has been completed, the anode layer of the cell was analyzed using SEM microscopy and Raman spectroscopy for any carbon deposition. High-magnification SEM in Fig. 9(e) shows the presence of carbon on Ni/YSZ anode with a composition of 17.3 atomic%. On the other hand, post-test HEA/GDC anode in Fig. 9(f) shows a clean and carbon-free surface. After 30 h of cell test, not only did the anode layer show remarkable carbon resistance, but good and stable contact were also formed between the anode layer and electrolyte. Fig. 9(d) shows the Raman spectra of two locations of the anode surface, one being the center and the other towards the edge of the anode layer. The absence of D and G bands at 1345 and 1595 cm^{-1}, respectively, suggests that the HEA/GDC anode was free of both amorphous and graphitic-typed carbons. HEA/GDC also exhibits high OSC, as suggested by TPD in Fig. 6(c), which can play an important role in the rapid oxidation of carbon to CO_x species, thus minimizing carbon poisoning. Fig. 10 shows a schematic depicting the role of coke-resistant HEA/GDC as oxygen vacancies in the anode enhance the mobility and diffusivity of oxygen ions to the anode surface to gasify any deposited carbon.

Conclusions

The HEA/GDC catalyst displayed promising potential as an anode material for internal utilization of CH_4 in SOFC. The bench top experiment suggested that HEA/GDC exhibits moderate reforming rate and excellent coking resistance under CH_4 reforming conditions, owing to the optimized mixture of HEA constituents and the high OSC of the GDC support. HEA/GDC also showed superior operational stability for CH_4 conversion over 30 h and post-test analysis of the catalyst did not indicate presence of carbon deposition, while both Ni/YSZ and Ni/GDC catalysts could be seen deactivating over time, despite the high initial CH_4 conversion and H_2 yield. The activity, stability and carbon-resistance of HEA/GDC as anode were also further investigated in a SOFC cell test. A current density of ~100 mA/cm^2 was achieved at 750 °C. The cell performed successfully over 30 h without any sign of decay. The overall polarization (ohmic and non-ohmic resistances) of the cell was low and stable. The moderate reforming rate of HEA/GDC is important for maintaining uniform temperature distribution and high coking tolerance especially for long-term high temperature SOFC operations, without compromising the electrochemical activity of the cell. Given the promising attributes of HEA/GDC as anode material in this study, successful effort has been made to further improve HEA/GDC for the direct utilization of other hydrocarbons such as methanol and ethanol, which are more easily stored and transported.

Declaration of competing interest

The authors declare that they have no known competing financial interests or personal relationships that could have appeared to influence the work reported in this paper.

Acknowledgements

Appendix A. Supplementary data

Supplementary data to this article can be found online at https://doi.org/10.1016/j.ijhydene.2022.09.018.

REFERENCES

[1] Da Paz Fiuza R, Aurélio Da Silva M, Boaventura JS. Development of Fe-Ni/YSZ-GDC electrocatalysts for application as SOFC anodes: XRD and TPR characterization and evaluation in the ethanol steam reforming reaction. Int J Hydrogen Energy 2010;35:11216—28.

[2] Laosiripojana N, Assabumrungrat S. Catalytic steam reforming of methane, methanol, and ethanol over Ni/YSZ: the possible use of these fuels in internal reforming SOFC. J Power Sources 2007;163:943—51.

[3] Angeli SD, Monteleone G, Giaconia A, Lemonidou AA. State-of-the-art catalysts for CH4 steam reforming at low temperature. Int J Hydrogen Energy 2014;39:1979—97.

[4] Peters R, Dahl R, Klüttgen U, Palm C, Stolten D. Internal reforming of methane in solid oxide fuel cell systems. J Power Sources 2002;106:238—44.

[5] Boder M, Dittmeyer R. Catalytic modification of conventional SOFC anodes with a view to reducing their activity for direct internal reforming of natural gas. J Power Sources 2006;155:13—22.

[6] Marina OA, Mogensen M. High-temperature conversion of methane on a composite gadolinia-doped ceria - gold electrode. Appl Catal Gen 1999;189:117—26.

[7] Saadabadi SA, et al. Solid oxide fuel cells fuelled with biogas: potential and constraints. Renew Energy 2019;134:194—214.

[8] Guo M, Ru X, Yang L, Ni M, Lin Z. Effects of methane steam reforming on the mechanical stability of solid oxide fuel cell stack. Appl Energy 2022;322:119464.

[9] Shiratori Y, et al. Study on paper-structured catalyst for direct internal reforming SOFC fueled by the mixture of CH4 and CO2. Int J Hydrogen Energy 2013;38:10542—51.

[10] Sugihara S, Iwai H. Experimental investigation of temperature distribution of planar solid oxide fuel cell: effects of gas flow, power generation, and direct internal reforming. Int J Hydrogen Energy 2020;45:25227—39.

[11] Wu H, et al. Ni-based catalysts for low temperature methane steam reforming: recent results on Ni-Au and comparison with other bi-metallic systems. Catalysts 2013;3:563—83.

[12] Chung YS, Kim H, Yoon HC, Chung JS, Sammes NM. Effects of manganese oxide addition on coking behavior of Ni/YSZ anodes for sofcs. Fuel Cell 2015;15:416—26.

[13] Nakagawa N, Sagara H, Kato K. Catalytic activity of Ni-YSZ-CeO2 anode for the steam reforming of methane in a direct internal-reforming solid oxide fuel cell. J Power Sources 2001;92:88—94.

[14] Wang L. Novel highly active Ni—Re super-alloy nanowire type catalysts for CO-free hydrogen generation from steam methane reforming. Bull Mater Sci 2020;43:3—5.

[15] Figen HE, Baykara SZ. Hydrogen production by partial oxidation of methane over Co based, Ni and Ru monolithic catalysts. Int J Hydrogen Energy 2015;40:7439—51.

[16] Wang Y, Yoshiba F, Kawase M, Watanabe T. Performance and effective kinetic models of methane steam reforming over Ni/YSZ anode of planar SOFC. Int J Hydrogen Energy 2009;34:3885—93.

[17] Meusinger J, Riensche E, Stimming U. Reforming of natural gas in solid oxide fuel cell systems. J Power Sources 1998;71:315—20.

[18] Thomas G. Overview of storage development. DOE Hydrogen Program Annual Review 2000. http://www1.eere.energy.gov/hydrogenandfuelcells/pdfs/storage.pdf. [Accessed 25 May 2022].

[19] Matsumura Y, Nakamori T. Steam reforming of methane over nickel catalysts at low reaction temperature. Appl Catal Gen 2004;258:107—14.

[20] Jabbour K, Massiani P, Davidson A, Casale S, El Hassan N. Ordered mesoporous "one-pot" synthesized Ni-Mg(Ca)-Al2O3 as effective and remarkably stable catalysts for combined steam and dry reforming of methane (CSDRM). Appl Catal B Environ 2017;201:527—42.

[21] Sehested J. Four challenges for nickel steam-reforming catalysts. Catal Today 2006;111:103—10.

[22] Christensen KO, Chen D, Lødeng R, Holmen A. Effect of supports and Ni crystal size on carbon formation and sintering during steam methane reforming. Appl Catal Gen 2006;314:9—22.

[23] Pashchenko D. Thermodynamic equilibrium analysis of steam methane reforming based on a conjugate solution of material balance and law action mass equations with the detailed energy balance. Int J Energy Res 2020;44:438—47.

[24] Pashchenko D, Makarov I. Carbon deposition in steam methane reforming over a Ni-based catalyst: experimental and thermodynamic analysis. Energy 2021;222:119993.

[25] Jabbour K. Tuning combined steam and dry reforming of methane for "metgas" production: a thermodynamic approach and state-of-the-art catalysts. J Energy Chem 2020;48:54—91.

[26] George EP, Raabe D, Ritchie RO. High-entropy alloys. Nat Rev Mater 2019;4:515—34.

[27] Pedersen JK, Batchelor TAA, Bagger A, Rossmeisl J. High-entropy alloys as catalysts for the co2 and co reduction reactions. ACS Catal 2020;10:2169—76.

[28] Harshini D, et al. Suppression of carbon formation in steam reforming of methane by addition of Co into Ni/ZrO2 catalysts. Kor J Chem Eng 2010;27:480—6.

[29] Choudhary VR, Rajput AM, Prabhakar B, Mamman AS. Partial oxidation of methane to CO and H2 over nickel and/or cobalt containing ZrO2, ThO2, UO2, TiO2 and SiO2 catalysts. Fuel 1998;77:1803—7.

[30] Ghungrud SA, Dewoolkar KD, Vaidya PD. Cerium-promoted bi-functional hybrid materials made of Ni, Co and hydrotalcite for sorption-enhanced steam methane reforming (SESMR). Int J Hydrogen Energy 2019;44:694—706.

[31] Huang TJ, Yu TC, Jhao SY. Weighting variation of water-gas shift in steam reforming of methane over supported Ni and Ni-Cu catalysts. Ind Eng Chem Res 2006;45:15—156.

[32] Kim H, Lu C, Worrell WL, Vohs JM, Gorte RJ. Cu-Ni cermet anodes for direct oxidation of methane in solid-oxide fuel cells. J Electrochem Soc 2002;149:A247.

[33] An W, Zeng XC, Turner CH. First-principles study of methane dehydrogenation on a bimetallic Cu/Ni(111) surface. J Chem Phys 2009;131.

[34] Lu XC, Zhu JH. Ni-Fe + SDC composite as anode material for intermediate temperature solid oxide fuel cell. J Power Sources 2007;165:678—84.

[35] Huang B, Wang SR, Liu RZ, Wen TL. Preparation and performance characterization of the Fe-Ni/ScSZ cermet anode for oxidation of ethanol fuel in SOFCs. J Power Sources 2007;167:288—94.

[36] Yao L, Galvez ME, Hu C, Da Costa P. Synthesis gas production via dry reforming of methane over manganese promoted nickel/Cerium-Zirconium oxide catalyst. Ind Eng Chem Res 2018;57:16645—56.

[37] Hadj-Sadok Ouaguenouni M, Benadda A, Kiennemann A, Barama A. Preparation and catalytic activity of nickel-manganese oxide catalysts in the reaction of partial oxidation of methane. Compt Rendus Chem 2009;12:740—7.

[38] Do JY, Park NK, Lee TJ, Lee ST, Kang M. Effective hydrogen productions from propane steam reforming over spinel-structured metal-manganese oxide redox couple catalysts. Int J Energy Res 2018;42:429—46.

[39] Lyu Z, Li H, Han M. Electrochemical properties and thermal neutral state of solid oxide fuel cells with direct internal reforming of methane. Int J Hydrogen Energy 2019;44:12151—62.

[40] Singh P, George RA, Shockling LA, Basel RA. Hydrocarbon reforming catalyst material and configuration of the same. US Pat; 1996. p. 5527631.

[41] Serincan MF, Pasaogullari U, Singh P. Controlling reformation rate for a more uniform temperature distribution in an internal methane steam reforming solid oxide fuel cell. J Power Sources 2020;468:228310.

[42] Trovarelli A. Catalytic properties of ceria and CeO2-Containing materials. Catal Rev - Sci Eng 1996;38:439—520.

[43] Yao HC, Yao YFY. Ceria in automotive exhaust catalysts. I. Oxygen storage. J Catal 1984;86:254—65.

[44] Bochentyn B, et al. Investigation of praseodymium and samarium co-doped ceria as an anode catalyst for DIR-SOFC fueled by biogas. Int J Hydrogen Energy 2020;45:29131—42.

[45] Andrade ML, Almeida L, do Carmo Rangel M, Pompeo F, Nichio N. Ni-catalysts supported on Gd-doped ceria for solid oxide fuel cells in methane steam reforming. Chem Eng Technol 2014;37:343—8.

[46] Nieva MA, Villaverde MM, Monzón A, Garetto TF, Marchi AJ. Steam-methane reforming at low temperature on nickel-based catalysts. Chem Eng J 2014;235:158—66.

[47] Ruckenstein E, Wang H. Carbon dioxide reforming of methane to synthesis gas over supported cobalt catalysts. Appl Catal Gen 2000;204:257—63.

[48] Ji L, Lin J, Zeng HC. Metal—Support interactions in Co/Al 2 O 3 catalysts: a Comparative study on reactivity of support. J Phys Chem B 2000;104:1783—90.

[49] Lucrédio AF, Assaf EM. Cobalt catalysts prepared from hydrotalcite precursors and tested in methane steam reforming. J Power Sources 2006;159:667—72.

[50] You X, et al. Ni-Co/Al2O3 bimetallic catalysts for CH4 steam reforming: elucidating the role of Co for improving coke resistance. ChemCatChem 2014;6:3377—86.

[51] Youn MH, et al. Hydrogen production by auto-thermal reforming of ethanol over Ni/γ-Al2O3 catalysts: effect of second metal addition. J Power Sources 2006;162:1270—4.

[52] Bernardo CA, Alstrup I, Rostrup-Nielsen JR. Carbon deposition and methane steam reforming on silica-supported NiCu catalysts. J Catal 1985;96:517—34.

[53] Khzouz M, Wood J, Pollet B, Bujalski W. Characterization and activity test of commercial Ni/Al2O 3, Cu/ZnO/Al2O3 and prepared Ni-Cu/Al 2O3 catalysts for hydrogen production from methane and methanol fuels. Int J Hydrogen Energy 2013;38:1664—75.

[54] Wang H, Ye JL, Liu Y, Li YD, Qin YN. Steam reforming of ethanol over Co3O4/CeO2 catalysts prepared by different methods. Catal Today 2007;129:305—12.

[55] Kan H, Lee H. Enhanced stability of Ni-Fe/GDC solid oxide fuel cell anodes for dry methane fuel. Catal Commun 2010;12:36—9.

[56] Koike M, et al. Catalytic performance of manganese-promoted nickel catalysts for the steam reforming of tar from biomass pyrolysis to synthesis gas. Fuel 2013;103:122—9.

[57] Choi JS, et al. Stable carbon dioxide reforming of methane over modified Ni/Al2O3 catalysts. Catal Lett 1998;52:43—7.

[58] Liu CJ, Ye J, Jiang J, Pan Y. Progresses in the preparation of coke resistant Ni-based catalyst for steam and CO 2 reforming of methane. ChemCatChem 2011;3:529—41.

[59] Rodemerck U, Schneider M, Linke D. Improved stability of Ni/SiO2 catalysts in CO2 and steam reforming of methane by preparation via a polymer-assisted route. Catal Commun 2017;102:98—102.

[60] Kapteijn F, Singoredjo L, Andreini A, Moulijn JA. Activity and selectivity of pure manganese oxides in the selective catalytic reduction of nitric oxide with ammonia. Appl Catal B Environ 1994;3:173—89.

[61] Ashok J, Kawi S. Nickel-iron alloy supported over iron-alumina catalysts for steam reforming of biomass tar model compound. ACS Catal 2014;4:289—301.

[62] He H, Dai HX, Wong KW, Au CT. RE0.6Zr0.4-xYxO2 (RE = Ce, Pr; X = 0, 0.05) solid solutions: an investigation on defective structure, oxygen mobility, oxygen storage capacity, and redox properties. Appl Catal Gen 2003;251:61—74.

[63] Klein JM, Hénault M, Roux C, Bultel Y, Georges S. Direct methane solid oxide fuel cell working by gradual internal steam reforming: analysis of operation. J Power Sources 2009;193:331—7.

[64] Li T, Chen D, Wang W, Liu C. Steam reforming of ethanol for hydrogen production over sandwich-structured Fe@G@M catalysts (M=Fe, Ni and Co). Mater Res Express 2019;6.

[65] Montero C, et al. Origin and nature of coke in ethanol steam reforming and its role in deactivation of Ni/La2O3-αAl2O3 catalyst. Ind Eng Chem Res 2019;58:14736—51.

[66] Trimm DL. Catalysts for the control of coking during steam reforming. Catal Today 1999;49:3—10.

[67] Guo T, et al. Effects of cobalt addition on the catalytic activity of the Ni-YSZ anode functional layer and the electrochemical performance of solid oxide fuel cells. ACS Appl Mater Interfaces 2014;6:16131—9.

[68] Yu S, Hu Y, Cui H, Cheng Z, Zhou Z. Ni-based catalysts supported on MgAl2O4 with different properties for combined steam and CO2 reforming of methane. Chem Eng Sci 2021;232:116379.

[69] Vecino-Mantilla S, Quintero E, Fonseca C, Gauthier GH, Gauthier-Maradei P. Catalytic steam reforming of natural gas over a new Ni exsolved ruddlesden-Popper manganite in SOFC anode conditions. ChemCatChem 2020;12:1453—66.